ECS Journal of Solid
State Science and
Technology

The Electrochemical Society
Advancing solid state & electrochemical science & technology

OPEN ACCESS

Comparison of Methods and Results for Determining Optical Characteristics of Bismuth Ferrite Thin Films Grown by Reactive Magnetron Co-Sputtering

To cite this article: Andrejus Litvakas and Aleksandras Iljinas 2025 *ECS J. Solid State Sci. Technol.* **14** 093006

View the article online for updates and enhancements.

You may also like

- PRISA: a user-friendly software for determining refractive index, extinction co-efficient, dispersion energy, band gap, and thickness of semiconductor and dielectric thin films
  S Jena, R B Tokas, S Thakur et al.
- Influence of Cu content on physical characterization and optical properties of new amorphous Ge–Se–Sb–Cu thin films
  H H Hegazy, A Dahshan and K A Aly
- On the Uniformity of Thin a-Si:H Films Prepared in an RF-Glow Discharge System
  G. Myburg and R. Swanepoel

ECC-Opto-10 Optical Battery Test Cell:
Visualize the Processes Inside Your Battery!

EL-CELL®
electrochemical test equipment

✓ **Battery Test Cell for Optical Characterization**
Designed for light microscopy, Raman spectroscopy and XRD.

✓ **Optimized, Low Profile Cell Design (Device Height 21.5 mm)**
Low cell height for high compatibility, fits on standard samples stages.

✓ **High Cycling Stability and Easy Handling**
Dedicated sample holders for different electrode arrangements included!

✓ **Cell Lids with Different Openings and Window Materials Available**

Scan me!

Contact us:
☎ +49 40 79012-734
✉ sales@el-cell.com
www.el-cell.com

Sample Test (Side-by-Side Setup)

Sample Test (Face-to-Face Setup)

This content was downloaded from IP address 193.219.34.13 on 23/09/2025 at 07:36

ECS Journal of Solid State Science and Technology, 2025 **14** 093006

Comparison of Methods and Results for Determining Optical Characteristics of Bismuth Ferrite Thin Films Grown by Reactive Magnetron Co-Sputtering

Andrejus Litvakas[z] and **Aleksandras Iljinas**

Department of Physics, Kaunas University of Technology, LT-51368 Kaunas, Lithuania

Bismuth ferrite (BFO) thin films were deposited by reactive magnetron co-sputtering in a pure oxygen environment at varying substrate temperatures in the range of 475 °C–550 °C in increments of 25 °C. As-deposited films were characterized for their structural, morphological and optical properties using X-ray diffraction (XRD), scanning electron microscopy (SEM), and optical absorption measurements. SEM and XRD analysis showed increase grain growth and crystallinity with increase of substrate temperature. Highest phase purity was observed in the sample grown at 500 °C and higher temperatures showed degraded phase purity with highest content of $Bi_2Fe_4O_9$ and β-Bi_2O_3. The optical band gap of BFO films varied in the range of 2.32–2.36 eV. The refractive index n(λ) was evaluated using Kramers-Kronig relations and the Swanepoel envelope method. Kramers-Kronig relations calculation showed a monotonic increase in n(λ) as opposed to Swanepoel envelope methods non-monotonic results. Transfer matric models confirmed that the values of n(λ) obtained by the Swanepoel envelope method align more closely to experimental transmittance spectra despite the samples weakly modulated spectra.

[DOI: 10.1149/2162-8777/ae020c]

Manuscript submitted June 6, 2025; revised manuscript received August 2, 2025. Published September 18, 2025.

Bismuth ferrite ($BiFeO_3$, BFO) thin films are known for their multiferroic properties which manifest as simultaneous ferroelectric and antiferromagnetic behavior at room temperature. BFO films also exhibit a wide optical band gap of 2.2 eV–2.7 eV and a high refractive index.[1–3] This makes BFO a suitable material for applications in spintronics, non-volatile memory devices, and photovoltaic systems.[4,5] The optical properties of BFO thin films are highly dependent on their crystal structure, stoichiometry, and surface morphology all of which are dependent on the deposition conditions, particularly the substrate temperature during growth.[6–8]

During film deposition by reactive magnetron co-sputtering the stoichiometry can be controlled account for bismuth volatility at higher substrate temperatures. This method also shows high deposition rates with strong adhesion to the substrate.[9,10] Typically, during reactive magnetron sputtering, the films are deposited using a mixture of oxygen/argon gas. However, an oxygen-rich environment allows the post-deposition annealing process to be skipped, decreasing the risk of phase segregation as well as the original dense structure achieved during deposition is preserved.[11–13]

To estimate the refractive index of thin films methods such as Kramers-Kronig relations (KK)[14,15] and the Swanepoel envelope method[16] can be used. The choice of method can significantly impact the accuracy and reliability of the calculated results. The Swanepoel envelope method relies on strong interference fringes in the transmittance spectrum, which makes the method sensitive to film thickness variations and also the surface roughness. The KK method can provide a more robust approach since the use of only the absorption data may be sufficient to derive the refractive index.[17–19]

While both Kramers-Kronig and Swanepoel envelope methods are widely used for optical characterization of thin films, direct comparisons between these techniques are rarely performed, particularly in cases where the transmittance spectra exhibit weak or poorly resolved interference fringes. This condition is common in oxide thin films with compositional or structural inhomogeneities. Most literature reports either apply one method in isolation or avoid films with weak modulation altogether. To our knowledge, this work is the first to perform a comparative evaluation of KK and Swanepoel methods for BFO films under weak interference conditions, supported by validation through transfer matrix modeling. This approach not only identifies the practical limitations of each method but also provides insight into their reliability and consistency with experimental data in challenging optical regimes. While functional studies such as piezoresponse or photocatalytic performance are of interest, this work focuses exclusively on the structural and optical properties of BFO thin films and the comparative evaluation of refractive index extraction methods.

In this work, BFO thin films were synthesized using a layer-by-layer reactive magnetron co-sputtering technique in a pure oxygen environment. The influence of substrate temperature during deposition on their structural, morphological, and optical properties was investigated. The optical characteristics of the films were determined using the Tauc plot method for the determination of the band gap and a comparison of optical characterization methods was performed. By comparing the optical characterization methods for determination of the refractive index, we aim to provide insights into their reliability and applicability in the context of weakly modulated transmittance spectra.

Experimental

Bismuth ferrite thin films were synthesized using a developed layer-by-layer direct current reactive magnetron co-sputtering technique. Soda–lime glass with a thickness of 1 mm (manufacturer: Nanoshel Company, Cheshire, UK) was used as a substrate. High-purity targets (Kurt J. Lesker Company, Dresden, Germany, 3 inches in diameter, disc-shaped, and with a purity of 99.9%) of single elements (Bi and Fe) were used for each magnetron. The starting pressure was 5×10^{-3} Pa. The chosen deposition temperatures were 475 °C, 500 °C, 525 °C, and 550 °C, with oxygen as the process gas, maintaining a working pressure of 1 Pa during deposition. The BFO films were then formed with deposition carried out in situ for a 1 h period. The deposition conditions of the films are summarized in Table I.

To examine the structural characteristics of the BFO films, X-ray diffraction (XRD) was performed using a Bruker D8 Advance diffractometer (Bruker, Billerica, MA, USA) with monochromatic CuKα radiation in Bragg–Brentano geometry. The average size of the thin-film crystallites was determined from peak broadening using single-line and multiple-line analysis. The surface morphology of the films was examined using a scanning electron microscope (S-3400N, Hitachi, Tokyo, Japan) at an operating voltage of 10 kV. The elemental distribution of Fe, Bi, and O in the films was analyzed via energy-dispersive spectroscopy using a Bruker Quad 5040 spectrometer (AXS Microanalysis GmbH, Hamburg, Germany).

[z] E-mail: andrejus.litvakas@ktu.edu

Table I. Deposition parameters and their values.

Deposition parameters	Values
Partial pressure of active O_2 gas, Pa	1
Target to substrate distance, cm	7
Applied voltage to target (Bi), V	250
Applied current to target (Bi), A	0.4
Applied voltage to target (Fe), V	250
Applied current to target (Fe), A	1
Substrate temperature, °C	475, 500, 525, 550

The transmittance spectra of the bismuth ferrite films were measured at normal incidence using a UV–VIS–NIR spectrophotometer (Ocean Optics USB4000, Ocean Optics, Inc., Dunedin, FL, USA) in the 380–780 nm range. The film thickness was measured using profilometry yielding values of 420 nm ± 10 nm. This thickness value was used throughout the band gap and optical modeling analysis. The refractive index of the thin films was calculated using two approaches: Kramers-Kronig (KK) relations and the Swanepoel envelope method.

Results and Discussion

The substrate temperature has a great effect on the surface morphology of BFO films. SEM images of the films grown at different temperatures (475 °C, 500 °C, 525 °C, and 550 °C) show a clear trend in grain evolution. Figure 1 shows the SEM images of the samples and the grain size distribution histograms are shown in Fig. 2. For each sample, the grain size distribution was evaluated from 100 individual grains. The mean values and standard deviations (σ) are reported in Fig. 2. The measurement uncertainty is estimated at ±5 nm, primarily due to image resolution limits and edge grain segmentation errors

At 475 °C, the film exhibits a fine-grained and relatively dense structure, with small crystallites distributed across the surface. The film exhibits the smallest average grain size (250.6 nm) with relatively low size dispersion ($\sigma = 1.19$). As the substrate temperature increases to 500 °C, the grains become more defined, indicating enhanced adatom mobility and improved crystallinity. There is an increase in average grain size to 337.9 nm, along with a slight rise in dispersion ($\sigma = 1.22$). As the substrate temperature increases to 525 °C a decrease in the average grain size is observed. The average size decreases to 314.5 nm with a further size dispersion increase ($\sigma = 1.28$). The deviation from the trend may reflect the prominent reappearance of secondary phases in the film as confirmed by XRD analysis. Secondary phases may have suppressed uniform growth of BFO that led to the increased grain size variability. At substrate temperature of 550 °C the average grain size increased to 383.2 nm with some grains forming elongated or irregular morphologies. This may suggest a possible change in growth mode or strain relaxation.[20–22] This sample showed the largest grain size dispersion ($\sigma = 1.29$).

All films exhibited continuous and crack-free surfaces, with grain size remaining in the range of 250.6 nm to 383.2 nm. The compact morphology and absence of drying-induced cracking is notable given the lack of any post-annealing treatment. In contrast, sol–gel methods, often produce porous or cracked films unless annealed carefully to relieve stress and promote densification.[23,24] The as-deposited morphology in our case reflects sufficient adatom mobility during growth. Higher substrate temperatures increase adatom mobility[25] that promote surface diffusion. The observed increase in grain size with temperature is attributed to this thermally activated diffusion processes, which promote crystallite coalescence and reduce the grain boundary density.[26] However, at higher temperatures, variations in morphology indicate that excessive thermal energy may influence film stress and defect formation.[27,28]

X-ray diffraction (XRD) was used to investigate the phase composition and crystallinity of BFO (BFO) thin films deposited

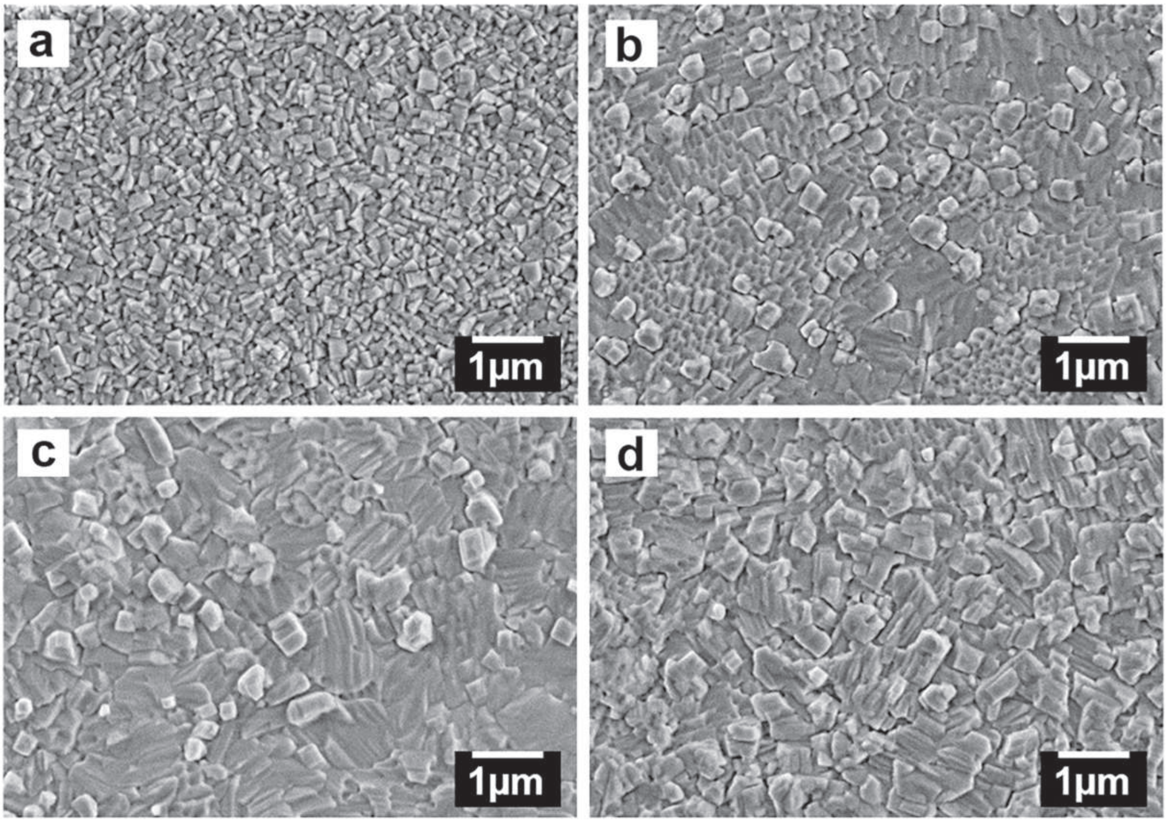

Figure 1. Scanning electron microscopy (SEM) images of BFO thin films deposited at substrate temperatures of 475 °C (a), 500 °C (b), 525 °C (c), and 550 °C (d). Progressive grain evolution is observed with increasing temperature.

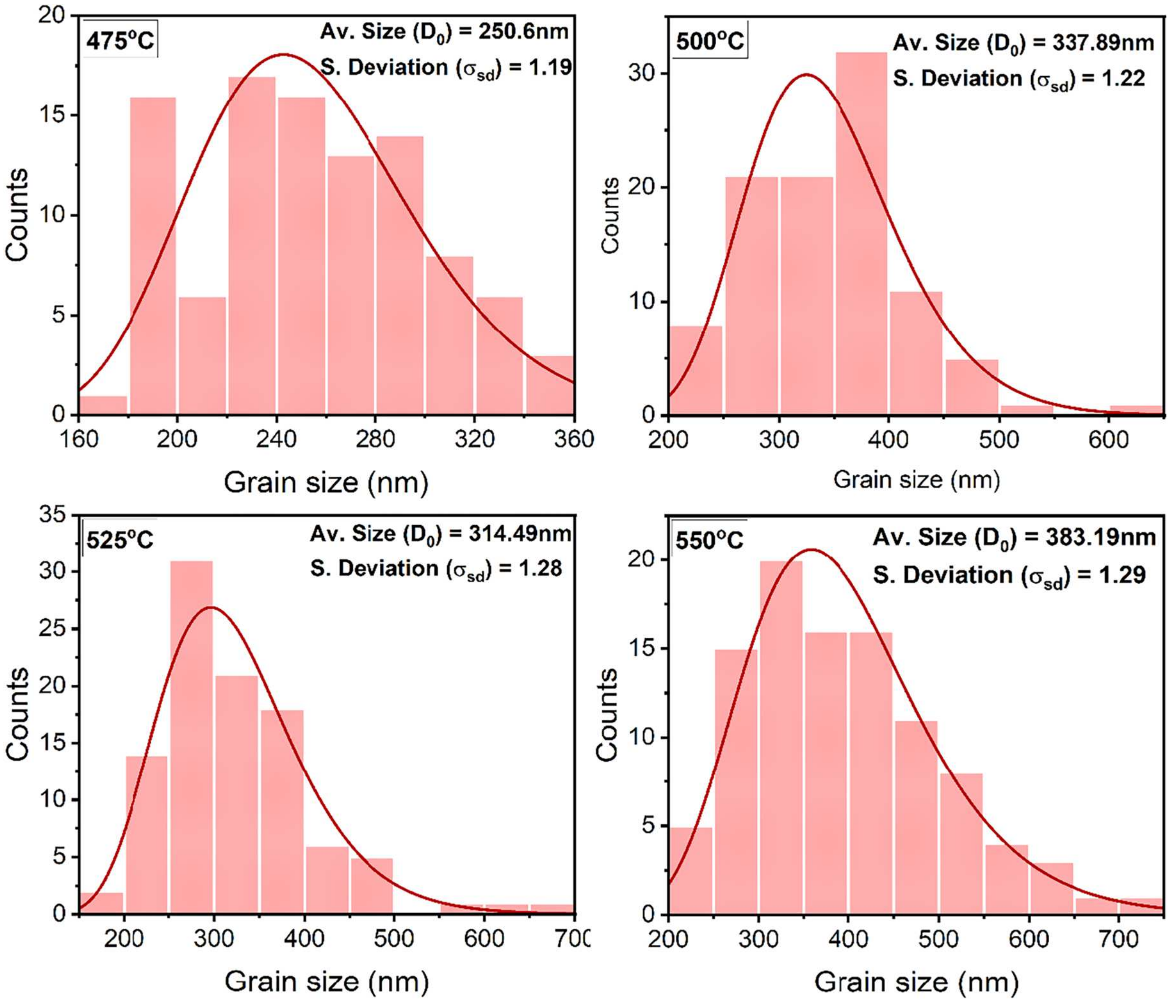

Figure 2. Grain size distribution histograms derived from SEM analysis for BFO films grown at various substrate temperatures. Each histogram is based on 100 measured grains.

at different substrate temperatures: 475 °C, 500 °C, 525 °C, and 550 °C. The resulting diffraction patterns are shown in Fig. 3, with peak positions corresponding to the rhombohedral perovskite BFO phase (R3c group no. 161) with lattice parameters of a = b = 5.59 Å, and c = 13.85 Å. (PDF:04-014-7267), and secondary phases identified as $Bi_2Fe_4O_9$ (PDF:01-072-1832) and β-Bi_2O_3 (PDF:04-015-6851). The XRD data were analyzed to determine crystallite size, using conventional Scherer's formula:

$$D = \frac{k\lambda}{\beta \cos\theta} \qquad [1]$$

where k = 0.9, λ is X-ray wavelength, θ is Bragg's angle, and β is the full width of diffraction line at half of the maximum intensity. The average crystallite size was 33 nm, 39 nm, 33 nm, and 45 nm for the 475 °C, 500 °C, 525 °C, and 550 °C respectively.

At substrate temperature of 475 °C, the BFO phase is formed, as evidenced by well-defined as evidenced by the (012), (104), (110), (006), and (024) reflections of rhombohedral BFO. At this temperature the (012) orientation is preferred. Secondary phase peaks of $Bi_2Fe_4O_9$ ($2\theta = 28.35°$) and β-Bi_2O_3 ($2\theta = 27.88°$ and 32.71°) are also present in the sample. Under lower-temperature conditions these prominent secondary phases suggest suppressed crystallization kinetics hinder the incorporation of Bi and Fe into the perovskite lattice.[29] This results in the unreacted species forming Bi-rich regions that crystallize as β-Bi_2O_3, and Fe-rich regions crystallize as $Bi_2Fe_4O_9$.[30] At 500 °C both the phase purity and crystallinity increases. The (012), (104), and (110) peaks corresponding to BFO are more intense and narrower compared to the sample grown at 475 °C. The peaks associated with $Bi_2Fe_4O_9$ ($2\theta = 28.35°$) and β-Bi_2O_3 ($2\theta = 27.88°$ and 32.71°) present in the 475° sample are substantially suppressed here, indicating a significant reduction in the concentration of these secondary phases. At 525 °C the (110) reflection of BFO is substantially diminished. Strong (012) and (104) BFO peaks are of similar in intensity and sharpness to those at 500 °C, indicating continued high crystallinity of these BFO orientations. However, the secondary phase peaks begin to reappear, particularly β-Bi_2O_3 ($2\theta = 27.88°$ and 32.71°), and a $Bi_2Fe_4O_9$ ($2\theta = 28.92°$). Also, an appearance of additional orientations of $Bi_2Fe_4O_9$ ($2\theta = 23.71°$ and 47.14°) is observed along with an emergence of unidentified phases at $2\theta = 23.04°$ and 34.98° marked in Fig. 3 by a star (*). The reemergence of these peaks along with an emergence of unidentified peaks suggests a temperature-induced destabilization of the single-phase BFO structure due to bismuth volatility at elevated temperatures. Even though the perovskite phase remains dominant, the onset of Bi loss compromises phase purity.[31] As the temperature of the substrate increases to 550 °C the BFO peaks remain intense and well-defined. A trend emerges showing that with the increase in substrate temperature BFO appears to prefer the (104) orientation under these conditions. However, at this elevated temperature the Bi-loss leads to the increase and reemergence of both $Bi_2Fe_4O_9$ ($2\theta = 23.71°$, 28.92°, and 47.14°) and β-Bi_2O_3 ($2\theta = 27.88°$, 32.71°, and 46.14°) secondary phases.

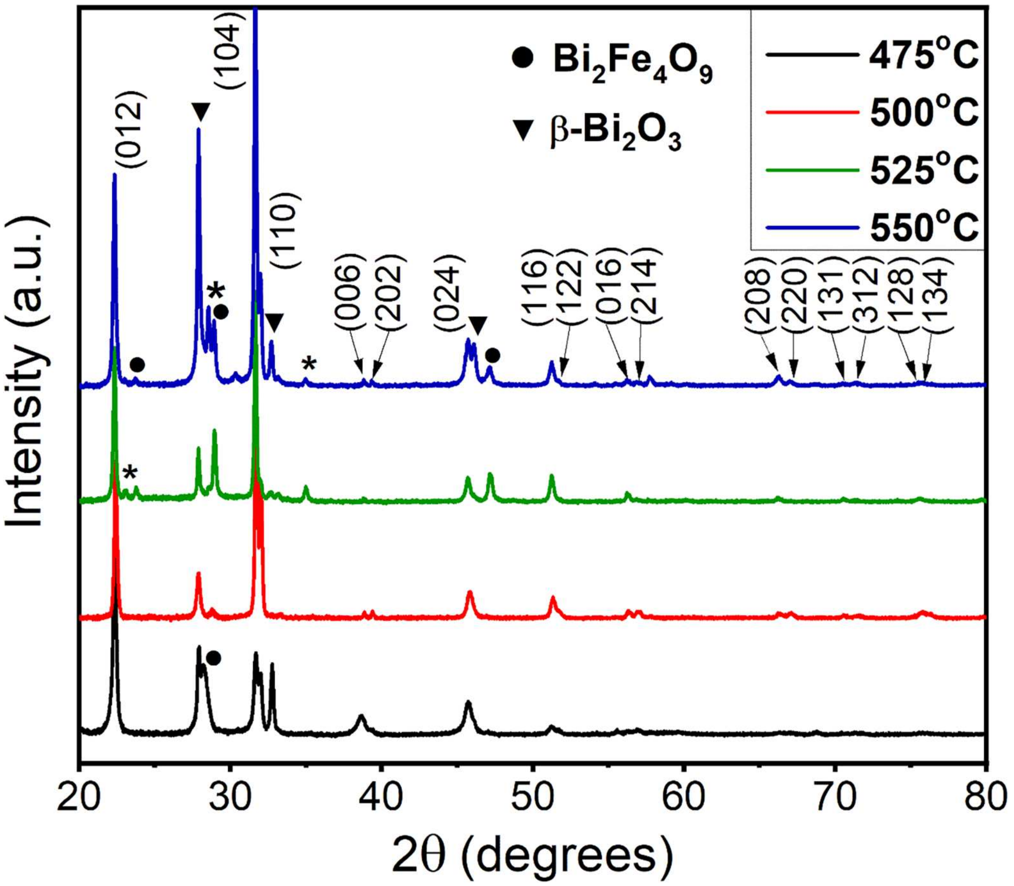

Figure 3. XRD patterns of BFO thin films deposited on glass substrates at different substrate temperatures. Peaks corresponding to the rhombohedral BFO phase (in parentheses) and secondary phases of $Bi_2Fe_4O_9$ (circle) and β-Bi_2O_3 (triangle) are indicated.

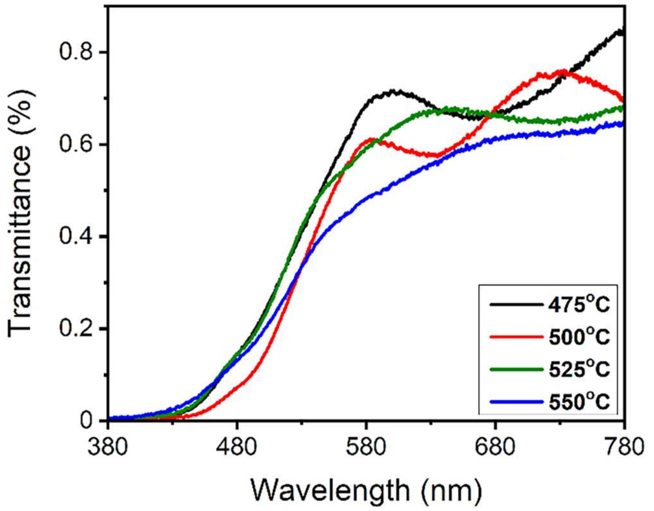

Figure 4. Optical transmittance spectra of BFO thin films deposited at varying substrate temperatures.

To quantify the relative phase composition in the films, Rietveld refinement was performed using HighScore Plus software. The phase concentrations for $BiFeO_3$, β-Bi_2O_3, and $Bi_2Fe_4O_9$ were extracted for all samples. The film deposited at 500 °C exhibited the highest $BiFeO_3$ content (76%), with 11% β-Bi_2O_3 and 13% $Bi_2Fe_4O_9$. In contrast, the 475 °C sample showed only 55% $BiFeO_3$, with elevated secondary phase content: 27% β-Bi_2O_3 and 18% $Bi_2Fe_4O_9$. The 525 °C and 550 °C samples also exhibited significant secondary phase presence, with $BiFeO_3$ fractions of 62% and 59%, respectively. These results confirm that while none of the films are fully phase-pure, the 500 °C deposition condition yields the highest degree of phase selectivity and minimal parasitic phase incorporation across the series.

The $BiFeO_3$ phase content peaks at 76% in the 500 °C sample, with the lowest concentration of secondary phases (β-Bi_2O_3 and $Bi_2Fe_4O_9$) across the series. This result, achieved without any post-deposition annealing, indicates a relatively high level of phase selectivity within a narrow thermal window. For context, sol–gel-derived BFO films typically require annealing at 600 °C or higher to reach comparable crystallinity and eliminate secondary phases,[32] while PLD-grown films achieve full perovskite purity at deposition temperatures above 700 °C.[33] Thus, although our films are not fully phase-pure, the structural outcome at 500 °C reflects efficient in situ phase formation enabled by reactive co-sputtering in a pure oxygen environment.

The XRD results suggest a non-monotonic relationship between phase purity and substrate temperature. An increase in substrate temperature typically leads to increased crystallinity. But since bismuth is volatile under high-temperature, low-pressure (vacuum) conditions elevated temperatures also promote Bi volatility which leads to the formation of secondary phases. Among the samples analyzed the sample grown at 500 °C substrate temperature shows the best balance between phase purity and crystallinity, yielding a nearly single-phase BFO film with minimal secondary phases. Thin BFO films deposited by reactive magnetron sputtering at relatively low substrate temperatures (around 450 °C–475 °C) tend to be poorly crystallized and often contain non-perovskite secondary phases.[34] As demonstrated by the 475 °C sample, lower substrate temperatures tend to hinder crystallization kinetics that lead to degraded phase purity.

The optical transmittance spectra of the BFO thin films are presented in Fig. 4. These measurements, recorded in the

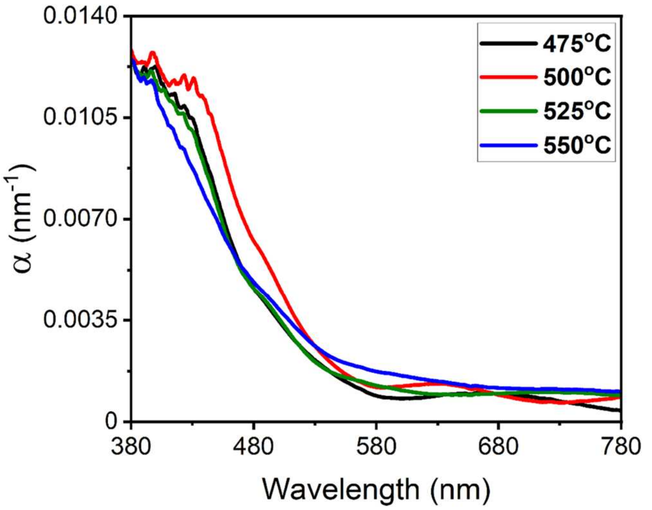

Figure 5. Absorption coefficient $\alpha(\lambda)$ for BFO thin films, calculated from UV–Vis absorbance data. The absorption edge is sharpest for the 500 °C film, indicating improved crystallinity and minimal defect-related absorption tails.

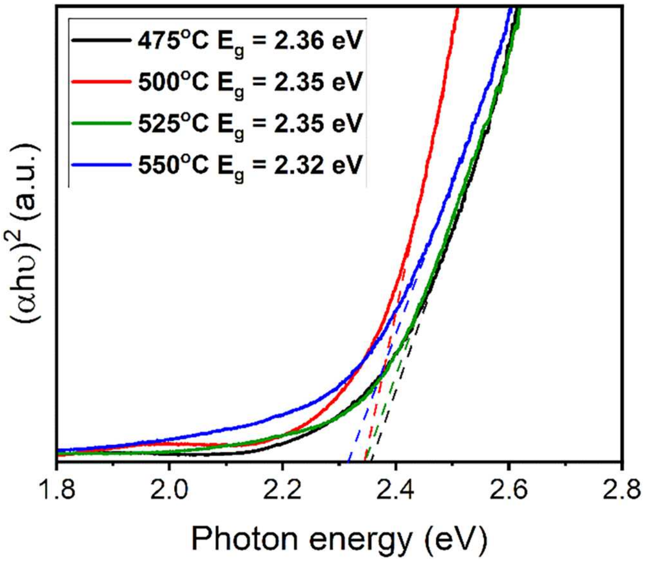

Figure 6. Tauc plots of $(\alpha h\nu)^2$ vs photon energy for BFO films, used to extract direct band gap values. Linear extrapolation indicates consistent band gap values across samples, with minimal deviation.

380–780 nm wavelength range, provide insight into the optical density, phase purity, and structural integrity of the films, which are closely linked to their microstructure and crystallographic features.

The 475 °C sample exhibits the highest overall transmittance. This high transmittance indicates a low optical absorption coefficient and density, consistent with the presence of secondary phases that either have larger band gaps or are sparsely distributed.[35] The 500 °C sample shows a reduced overall transmittance along with an increase in absorbance in the ~400–550 nm range. As the XRD data confirmed this sample exhibits enhanced crystallinity and suppression of secondary phases at this temperature. higher structural order, denser film morphology, and higher optical path lengths within well-crystallized grains can lead to stronger light–matter interactions increasing absorbance.[36,37] A reduction and smearing of the transmittance curve are observed in the and 550 °C and 550 °C samples, with the 550 °C sample exhibiting the strongest optical attenuation. The broader absorption tail is consistent with increased sub-gap absorption, which can be attributed to Urbach-type behavior resulting from due to high thermal energy induced defects.[38] Structural findings support the increased absorption with an increase in secondary phase intensity, and possible defect formation due to Bi volatility. Even though the crystallinity remains high at these temperatures the excess thermal energy that can promote secondary phase segregation, which introduces optical scattering and non-radiative losses.

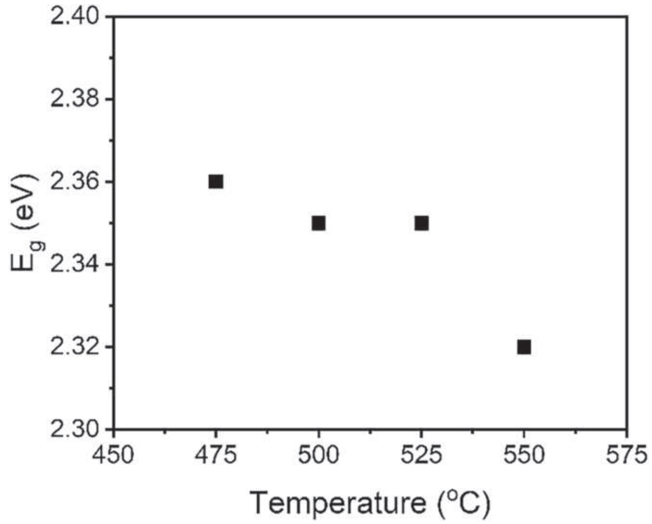

Figure 7. Variation of optical band gap energy with substrate temperature. The deviation by 40 meV fall within analytical uncertainty, suggesting the band structure of BFO remains stable over the investigated temperature range.

Among the samples, the film deposited at 500 °C demonstrates the most favorable combination of high phase purity, controlled morphology, and moderate optical density, making it the optimal condition for applications requiring transparent or photoresponsive BFO thin films.

The band gap of semiconductors can be one of two types: direct and indirect band gap. The minimum energy of the electrons in the conduction band and the maximum energy in the valence band are characterized by crystal momentum, k-vector, in the Brillouin zone. To evaluate the optical absorption edge of the BFO films, we employed the Tauc plot method on the UV–vis transmittance data assuming a direct allowed transition. For each sample, the absorption coefficient α (Fig. 5) was calculated from the absorption data and film thickness using the expression:

$$\alpha(\lambda) = 2.303\frac{\mathrm{A}(\lambda)}{\mathrm{d}} \qquad [2]$$

where A(λ) is the absorbance, and d is the film thickness. A Tauc plot of $(\alpha h\nu)^2$ vs photon energy was constructed assuming a direct allowed transition.

The Tauc plots showed a linear region just above the absorption edge, from which the direct optical band E_g was obtained by extrapolating to the intercept of the photon energy axis. The resulting curves are shown in Fig. 6. All samples exhibit a well-defined absorption onset in the visible region, confirming the wide band gap semiconducting nature of the BFO phase. To account for uncertainty in the band gap extraction, each Tauc plot was fitted over multiple linear regions near the absorption edge, and the standard deviation of the extrapolated intercepts was determined. The resulting uncertainty in the band gap values is estimated at ±0.02 eV. This variation reflects the subjectivity in selecting the linear fitting range and the influence of spectral noise.

The extracted band gaps fall within a narrow range of 2.32–-2.36 eV, with only slight variation across the series. The band gap values were plotted as E_g vs substrate temperature in Fig. 7. The slight variations in the band gap are within the expected margin of

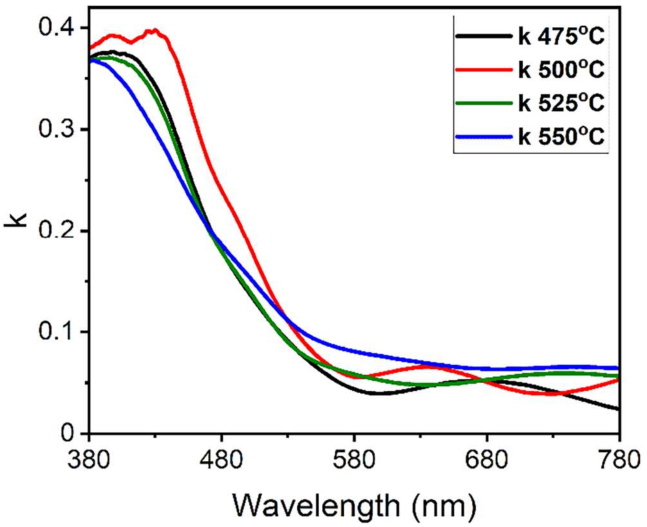

Figure 8. Extinction coefficient k(λ) of BFO films calculated from UV–vis absorbance data.

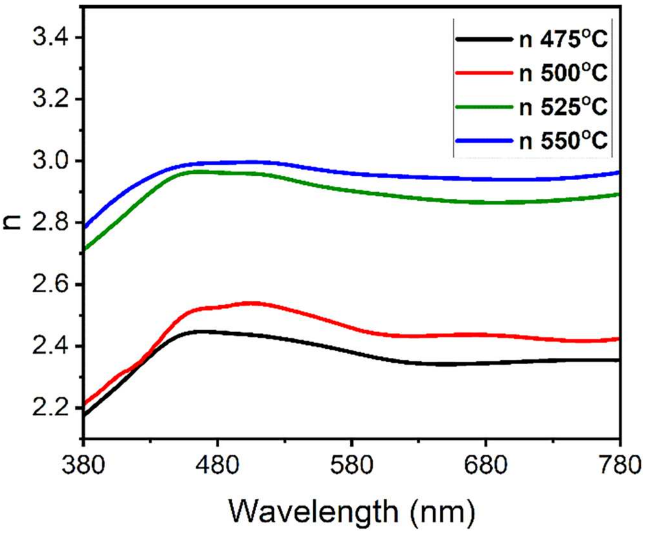

Figure 9. Refractive index dispersion curves obtained from Kramers-Kronig analysis for BFO films. A monotonic increase in refractive index with substrate temperature is observed.

error associated with Tauc plot extrapolation. The linear slope region of the $(\alpha h\nu)^2$ plot can be influenced by data noise, uncertainty in film thickness measurements, and the subjectivity in selecting the fitting range. The 40 meV difference between the extreme values (2.32 eV and 2.36 eV) is likely not indicative of a true band gap modulation but rather reflects analytical uncertainty. This reinforces that the electronic structure of the BFO phase remains essentially stable within this temperature window, and no significant temperature-induced band structure alteration occurs in the absence of extreme phase decomposition. These band gap values fall within the expected range[39] for BFO films prepared by high-temperature PLD or annealed sol–gel methods, indicating that our films achieve comparable optical behavior despite lower thermal input and the absence of post-deposition crystallization steps.

The KK analysis was conducted using the absorbance-derived extinction coefficient k(λ), calculated from UV–vis transmission data over the spectral range of 380–780 nm.

Where A is the absorption at a given wavelength, and d is the film thickness. The film thicknesses were measured independently by profilometry. From this, the extinction coefficient k(λ) was calculated as:

$$\mathrm{k}(\lambda) = \frac{\alpha(\lambda)\lambda}{4\pi} \qquad [3]$$

The calculated extinction coefficient k(λ) can be seen in Fig. 8. Subsequently, n(λ) was obtained by numerically evaluating the KK integral, which connects the real and imaginary parts of the complex refractive index through:

$$\mathrm{n}(\omega) - 1 = \frac{2}{\pi}\mathrm{P}\int_0^{\infty} \frac{\omega'\mathrm{k}(\omega')}{\omega'^2 - \omega^2}\mathrm{d}\omega' \qquad [4]$$

where P denotes the Cauchy principal value. Since only the absorption data was used, the accuracy of n(λ) depends directly on the precision and spectral completeness of the extinction coefficient k(λ), especially near the absorption edge. Since the KK method used in this study relies entirely on the absorption spectrum, any inaccuracies in $\alpha(\lambda)$ or film thickness directly propagate into the real part of the refractive index. While the KK approach offers a causally consistent framework linking k and n, its reliance on complete absorption spectra and sensitivity to numerical extrapolation can lead to overestimation of n(λ) in strongly absorbing or defect-rich samples,[40] as observed in the 525 °C and 550 °C films. Using the KK analysis, we obtained the spectral dispersion of the refractive index n(λ) and the extinction coefficient k(λ) for the BFO thin films. Figure 9 illustrates the refractive index dependency on wavelength for the four samples.

The refractive indices were also calculated by the Swanepoel envelope method. Usually, this method can be applied to films exhibiting clear, periodic interference fringes. These fringes arise from constructive and destructive interference between parallel film surfaces. However, in this study, the transmittance spectra of the BFO films exhibited only weak and modulation, especially for the samples grown at higher substrate temperatures (525 °C and 550 °C). This fringe suppression is attributed to moderate absorption in the visible range, film roughness, and compositional inhomogeneity. These conditions are common in oxide films with secondary phases present.

Despite these limitations, Swanepoel envelope method was still employed. The envelope curves were constructed using a minimal set of visually selected extrema that showed consistent curvature and spacing relative to the overall trend. When only one extremum was available, the surrounding spectral shape was used to guide the extrapolation of the envelope's trajectory under the assumption of a slowly varying interference pattern. Third-order polynomial fits were then applied to these manually selected points to generate continuous upper and lower envelope functions. This approach, while approximate, allows for a physically reasonable reconstruction of the interference envelope and enables the use of the Swanepoel method even in the absence of fully developed fringes.

Even though the envelopes were constructed approximately, in some cases with only one visible extremum and guided by visual estimation—the refractive index values calculated from these envelopes showed physically reasonable behavior. The calculated n(λ) values followed smooth, non-erratic trends across the spectral range, did not show artificial jumps or noise amplification, and aligned with expectations from film morphology and known material properties. Because of this, the approximated envelopes despite being based on sparse data still yielded meaningful optical constants. The refractive index n(λ) was then calculated from these envelopes (Fig. 10). The refractive index n(λ) was then calculated from these envelopes.

Given the weak modulation of transmittance, uncertainty in envelope identification introduces a refractive index estimation error of approximately ±0.05 in the transparent spectral region. This was estimated by varying the envelope trace by ±2% and recalculating n(λ). The refractive index at a given wavelength was calculated using the relation:

$$\mathrm{n}(\lambda) = [\mathrm{N} + \sqrt{\mathrm{N}^2 - \mathrm{s}^2}\,]^{0.5} \qquad [5]$$

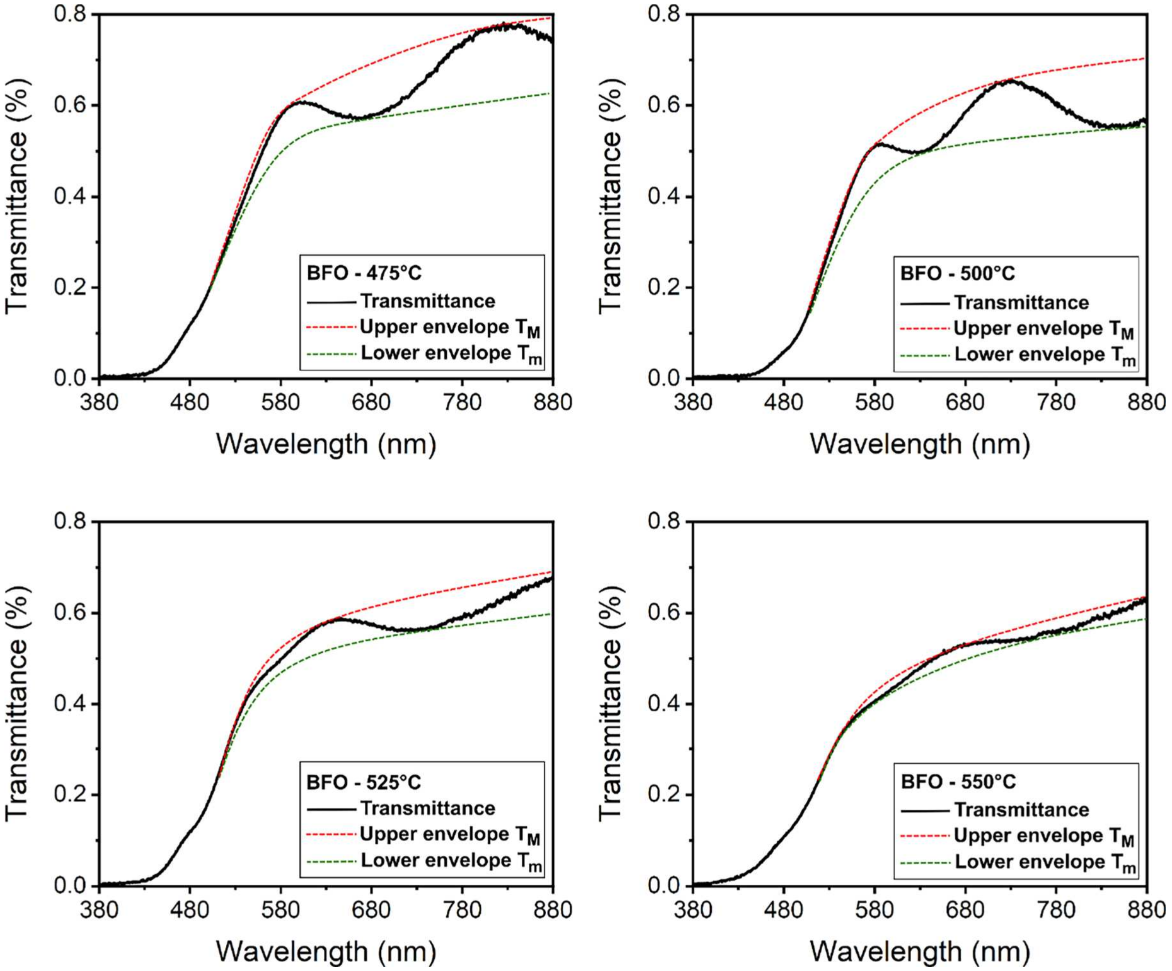

Figure 10. Constructed transmittance envelopes for BFO thin films using the Swanepoel method. Due to weak interference fringes, envelope curves were estimated from visually selected extrema and fitted using third-order polynomials to approximate upper and lower bounds for refractive index calculation.

where

$$N = \frac{2sT_m}{T_m - T_M} + \frac{s^2 + 1}{2} \qquad [6]$$

here, T_M and T_m are the transmittance maxima and minima respectively, and s is the refractive index of the substrate. The calculated refractive index values are shown in Fig. 11. Values were calculated in the 500–780 nm range due to difficulties of fitting the upper and lower envelopes below 500 nm.

The refractive index curves obtained through the KK method show a monotonic increase of the refractive index with substrate temperature. The 475 °C film shows the lowest refractive index (2.17–2.45), while the 550 °C film reaches a peak value of 3. At first glance the trend of increasing n(λ) can be interpreted as caused by increased crystallinity, grain growth, and the increase in optical density. However, the transfer matrix models contradict this interpretation.

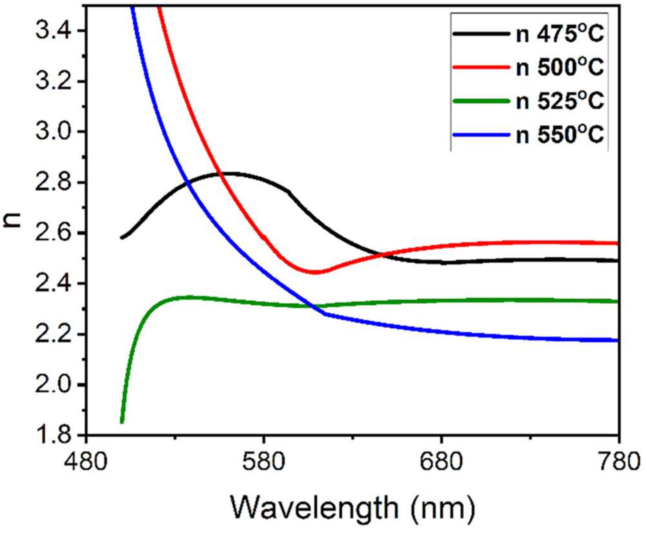

Figure 11. Refractive index dispersion calculated using the Swanepoel envelope method. A non-monotonic variation in refractive index with substrate temperature is observed.

In the Swanepoel-derived n(λ) values in the range from 500 nm to ~580 nm the approximate nature of the envelope fitting brings uncertainties in the results due to the imprecise convergence of the envelopes in this range. Above this range the curves of n(λ) (Fig. 11) exhibit a non-monotonic trend with substrate temperature, except for the sample grown at 500 °C. As this sample was composed of minimal secondary phases and exhibited high crystallization, this curve may represent the pure BFO film refractive index due to minimal influence of the secondary phases. In films with an optical resonance condition, where improved film crystallinity and minimal light-scattering loss coinciding with interference optimization, can lead to artificially elevated n(λ) values using the envelope method. This effect has been reported in films with strongly varying absorption or spatial inhomogeneity near optimal growth conditions.[16] This trend diverges from the monotonic increase in n

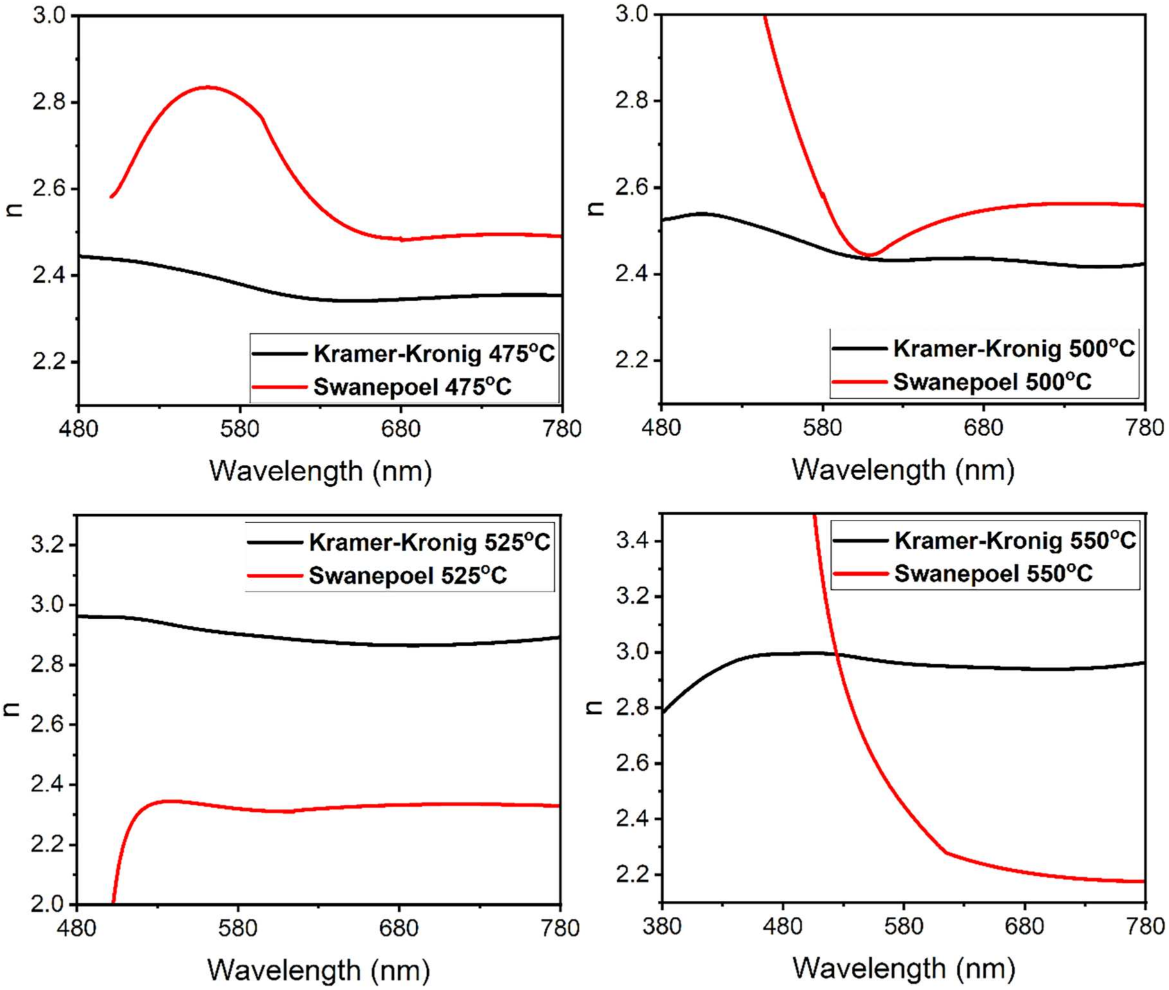

Figure 12. Comparison of refractive index values obtained via Kramers-Kronig and Swanepoel envelope methods. While KK-derived values increase monotonically with temperature, Swanepoel-derived n(λ) captures the non-monotonic trend reflective of structural degradation at higher temperatures.

obtained via the (KK) method and from expectations based on film density or crystallinity alone. The comparison of the curves is shown in Fig. 12.

To validate the results obtained from both methods transfer matrix modeling (TMM) was performed. The experimentally measured transmittance spectrum of each film was fitted using a multilayer optical model (air/film/glass). To determine which of the two methods produced the best fitting transmittance curve to the experimentally obtained transmittance data of the films we used the output values of the Swanepoel envelope method and KK method as input data for the transfer matrix modelling.

The first dataset included the real part of the refractive index that was obtained from the Swanepoel envelope method calculations and the extinction coefficient values were calculated from the experimentally obtained absorbance data. The second dataset was obtained from the KK calculations, where both n and k were calculated from the absorbance data. The modelled theoretical transmittance curves were compared with the experimental transmittance curves in Fig. 13. The model assumed a single BFO layer of 420 nm thickness, as measured experimentally. No thickness fitting was performed; instead, the measured values were fixed to avoid artificial compensation for refractive index or extinction coefficient deviations.

Both input datasets resulted in transmittance spectra of similar shape to the experimental data. However, when Swanepoel-derived optical constants are used as input for the TMM simulations, the resulting transmittance spectra closely match experimental data, while KK-derived values tend to overshoot the experimental values by as much as 20%. This indicates that the Swanepoel envelope method provides more physically representative n values despite difficulties fitting the envelopes. This practical agreement reinforces the utility of Swanepoel's method even in the absence of well-defined interference fringes, as long as the envelope extraction remains internally consistent.

The refractive index values obtained via Swanepoel and KK methods diverge not only in trend but in physical plausibility across the temperature series. As temperature increases, KK predicts a steady increase in n even at 525 °C and 550 °C, where structural data shows reemergence of secondary phases and potentially increased roughness. This is physically inconsistent since increased disorder and phase separation should suppress coherent light propagation, reducing effective refractive index. The KK results thus fail to reflect the optical degradation evidenced by both decreased transmittance and increasing Urbach tails in absorption.

The drop in refractive index, calculated by Swanepoel envelope method, at 525 °C and 550 °C correlates with the onset of Bi volatility, increased parasitic phase content (notably $Bi_2Fe_4O_9$ and β-Bi_2O_3), and grain boundary disorder, all of which increase scattering and reduce refractive contrast. The high n at 500 °C is also supported by structural data: this sample exhibits the highest phase purity and crystallinity, leading to enhanced refractive contrast and strong light–matter interaction. While its optical loss is not the lowest in the series, it reflects a balance between transmission and refractive coherence - unlike the 525 °C and 550 °C samples, where optical density increases due to scattering, defect states, and parasitic absorption. Hence, Swanepoel's non-monotonic n profile maps accurately onto the full set of structural (XRD), morphological

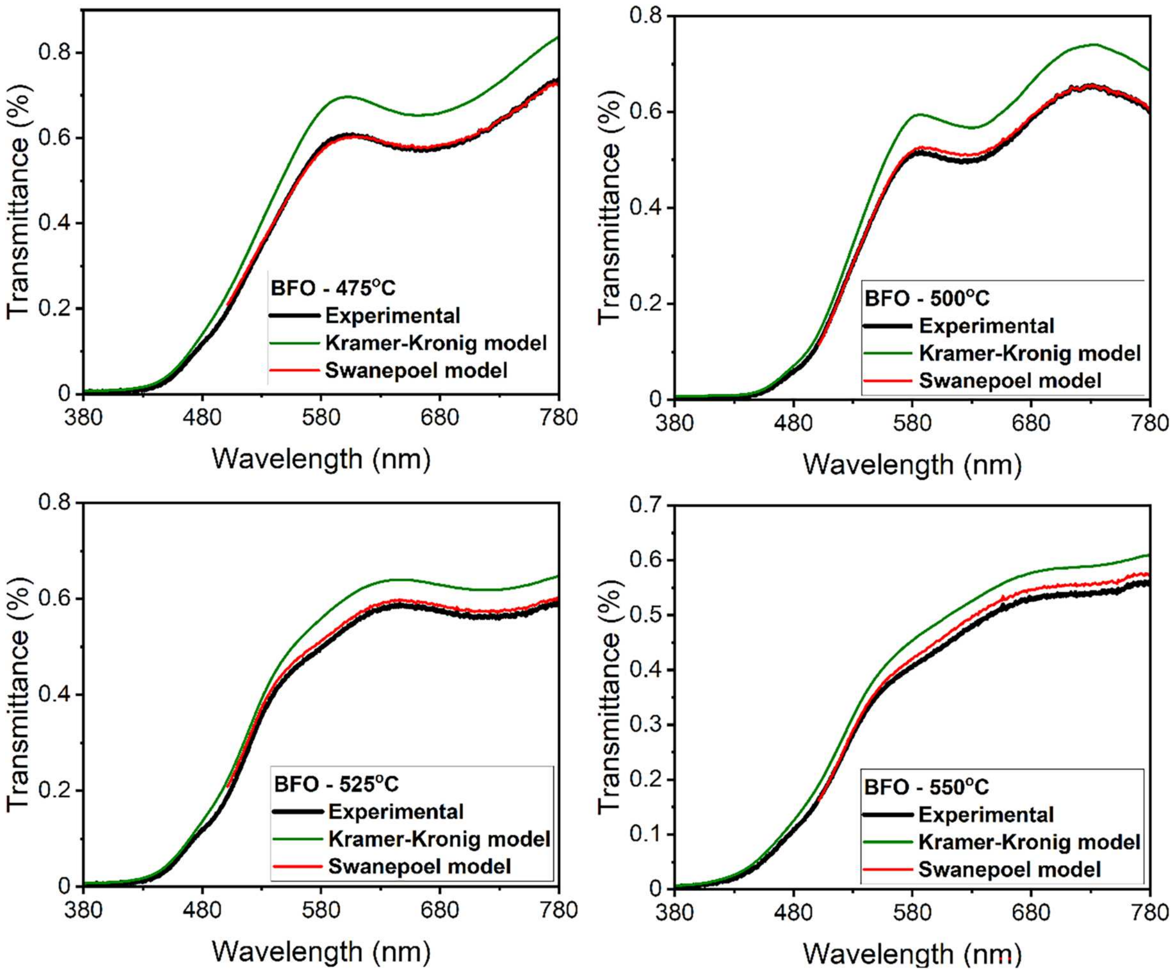

Figure 13. Transfer matrix modeling (TMM) results comparing modeled and experimental transmittance spectra. The Swanepoel-derived optical constants yield a better match to experimental data, validating its use despite weak interference fringes.

(SEM), and optical data, while the KK results misrepresent the effects of high-temperature degradation.

Conclusions

BFO thin films were successfully grown by reactive magnetron co-sputtering technique in a pure oxygen environment without post-annealing of the samples. The substrate temperature of 475 °C resulted in poor crystallinity, while the film grown at 500 °C exhibited high crystallinity, minimal secondary phase content (76% BFO), dense and crack-free morphology, and a good optical response. At higher substrate temperatures of 525 °C and 550 °C high crystallinity was observed, but the onset of Bi loss led to severe phase degradation with an increase in secondary phases ($Bi_2Fe_4O_9$ and β-Bi_2O_3). Despite the presence of secondary phases, the 500 °C sample shows a well-crystallized BFO-rich film with good optical quality and dense morphology, all achieved without post-deposition annealing. These results confirm that reactive co-sputtering in pure oxygen, without the need for argon gas, provides a viable pathway for BFO film fabrication, with fewer processing steps, and in situ phase formation at lower thermal budgets than typical PLD or sol–gel methods.

The refractive index, extracted from both the Swanepoel envelope method and Kramers-Kronig relations, was used as input for the transfer matrix modeling to produce theoretical transmittance spectra of the samples. When values obtained from the Swanepoel envelope method were used as input for the transfer matrix, the resulting spectra aligned more closely to experimental data, while values obtained from KK method overestimated the transmittance. These results demonstrate the practical reliability of the Swanepoel method, even under suboptimal fringe visibility, and highlight its utility in thin-film systems where weak interference and compositional inhomogeneity often occur. These findings are particularly relevant for the integration of BFO thin films in applications such as transparent optoelectronics, photovoltaics, and non-volatile memories, where accurate optical modeling and low-temperature processing are critical.

ORCID

Andrejus Litvakas https://orcid.org/0009-0006-2671-2999

References

1. N. Wang, X. Luo, L. Han, Z. Zhang, R. Zhang, H. Olin, and Y. Yang, *Nano-Micro Lett.*, **12**, 81 (2020).
2. A. Bismibanu, P. R. Vanga, T. Selvalakshmi, M. Ashok, and M. Alagar, *J. Electron. Mater.*, **47**, 6373 (2018).
3. J. Ding, H. X. Li, G. Li, J. Tu, J. Tian, and L. Zhang, *Inorg. Chem. Front.*, **10**, 1215 (2023).
4. K. Sharma and A. Singh, *J. Adv. Chem. Sci.*, **2**(2), 241 (2016).
5. A. Sasmal, A. Patra, S. Maity, S. K. Pratihar, and S. Sen, *Sustain. Energy Fuels*, **6**, 4652 (2022).
6. E. Ching-Prado, H. Miranda, and E. de Obaldia, *Ferroelectrics*, **611**, 25 (2023).
7. M. H. M. Abdelrehman, V. Craciun, R. E. Kroon, A. Yousif, and H. A. A. S. Ahmed, *Physica B: Condens. Matter*, **581**, 411757 (2020).
8. A. Anjum, R. Ahmed, Z. A. Umar, S. Azzam, T. Hussain, M. Sarwar, and M. A. Baig, *Physica B: Condens. Matter*, **644**, 414195 (2022).
9. S. J. Joo, B. S. Kim, B. K. Min, M. W. Oh, J. E. Lee, B. Ryu, H. W. Lee, and S. D. Park, *J. Nanosci. Nanotechnol.*, **15**, 8299 (2015).
10. M. Ratova, P. Kelly, G. T. West, X. Xia, and Y. Gao, *Materials*, **9**, 67 (2016).
11. S. E. Nunes, L. C. Matte, and C. R. da Cunha, *Mater. Res. Express*, **6**, 095905 (2019).

12. M. L. V. Mahesh, A. R. James, and V. V. B. Prasad, *J. Mater. Sci., Mater. Electron.*, **26**, 4930 (2015).
13. M.-J. Park, W.-H. Lee, K. Kim, D.-J. Yun, and S. M. Yoon, *Electron. Lett.*, **52**, 853 (2016).
14. R. de L. Kronig, *J. Opt. Soc. Am.*, **12**, 547 (1926).
15. A. Kramers, “Scattering of radiation by atoms.” *Collected Scientific Papers* (North-Holland Publishing Co., Amsterdam)17, 545–558 (1956).
16. R. Swanepoel, *J. Phys. E: Sci. Instrum.*, **17**, 896 (1984).
17. G. Lu, Z. Shen, H. Wang, L. Bu, and G. Lu, *Rev. Sci. Instrum.*, **94**, 023907 (2023).
18. B. Jin, Z. Song, Y. Jia, C. Zhang, X. Lin, S. Wang, and Dai, *Opt. Express*, **25**, 440 (2017).
19. I. Konstantinov, T. Babeva, and S. Kitova, *Appl. Opt.*, **37**, 4260 (1998).
20. M. G. Cho, K. Sytwu, L. R. DaCosta, C. Groschner, M. H. Oh, and M. C. Scott, *ACS Nano*, **18**, 29736 (2024).
21. W. Brückner, V. Weihnacht, W. Pitschke, J. Thomas, and S. Baunack, *J. Mater. Res.*, **15**, 1062 (2000).
22. S. Y. Liu, Q. P. Cao, Q. Yu, X. D. Wang, D. X. Zhang, and J. Z. Jiang, *J. Non-Cryst. Solids*, **510**, 112 (2019).
23. E. J. Kappert, D. Pavlenko, J. Malzbender, A. Nijmeijer, N. E. Benes, and P. A. Tsai, *Soft Matter*, **11**, 882 (2015).
24. F. Boulogne, F. Giorgiutti-Dauphiné, and L. Pauchard, *Oil Gas Sci. Technol.*, **69**, 397 (2014).
25. S. B. Patel, C. Li, A. Al-Mahboob, J. T. Sadowski, and G. Zhou, *J. Am. Chem. Soc.*, **147**, 1656 (2025).
26. R. T. Wang, C. Y. Ma, J. R. Li, P. H. Liu, F. W. Qin, N. Zhou, and Q. Y. Zhang, *Vacuum*, **225**, 113224 (2024).
27. B.-C. Jeon, S. C. Chae, T. D. Kang, and S. J. Moon, *J. Korean Phys. Soc.*, **64**, 1849 (2014).
28. V. Das and N. Jayaprakash, *J. Vac. Sci. Technol.*, **20**, 58 (1982).
29. C. Wesley, L. Bellcase, J. S. Forrester, E. C. Dickey, I. M. Reaney, and J. L. Jones, *J. Am. Ceram. Soc.*, **107**, 3716 (2024).
30. A. Kirsch, G. B. Strapasson, N. Lefeld, M. Gogolin, M. C. Videbæk, S. Banerjee, H. N. Bordallo, and K. M. Ø. Jensen, *Chem. Mater.*, **37**, 338 (2024).
31. H. R. Yan, N. F. Ding, G. Wu, P. X. Yang, J. H. Chu, and H. M. Deng, *Mater. Sci. Forum*, **745**, 131 (2013).
32. P. Dash, B. N. Dash, H. Rath, C. Rath, and N. C. Mishra, *Indian J. Phys.*, **83**, 485 (2009).
33. N. Pavlovic, J. D’Haen, H. Modarresi, A. Riskin, C. Dobbelaere, M. Van Bael, K. Temst, A. Hardy, and M. Van Bael, *J. Mater. Sci.*, **50**, 493 (2015).
34. S.-S. Park, *Korean J. Mater. Res.*, **19**, 253 (2009).
35. C.-C. Yu, H. Chang, A.-C. Sun, and J.-W. Chiou, *Vacuum*, **169**, 108918 (2019).
36. S. K. Srivastav and N. S. Gajbhiye, *J. Am. Ceram. Soc.*, **95**, 3678 (2012).
37. K. Sarkar, S. Mukherjee, and M. K. Mitra, *J. Inst. Eng. (India) Ser. D*, **95**, 135 (2014).
38. S. Hao, M. Hetzl, V. F. Kunzelmann, S. Matich, Q. Sai, C. Xia, I. D. Sharp, and M. Stutzmann, *Appl. Phys. Lett.*, **116**, 092102 (2020).
39. D. H. Wallis and N. C. Wickramasinghe, *Astrophys. Space Sci.*, **262**, 193 (1998).
40. D. Sando, C. Carrétéro, M. N. Grisolia, A. Barthélémy, V. Nagarajan, and M. Bibes, *Adv. Opt. Mater.*, **6**, 1700836 (2018).